# Space-time landslide hazard modeling via Ensemble Neural Networks

Ashok Dahal[1*], Hakan Tanyas[1], Cees van Westen[1], Mark van der Meijde[1], P. Martin Mai[2], Raphael Huser[3], Luigi Lombardo[1]

## Abstract

For decades, a full numerical description of the spatio-temporal dynamics of a landslide could be achieved only via physics-based models. The part of the geomorphology community focusing on data-driven model has instead focused on predicting where landslides may occur via susceptibility models. Moreover, they have estimated when landslides may occur via models that belong to the early-warning-system or to the rainfall-threshold themes. In this context, few published research have explored a joint spatio-temporal model structure. Furthermore, the third element completing the hazard definition, i.e., the landslide size, has hardly ever been modeled over space and time. However, the technological advancements of data-driven models have reached a level of maturity that allows to model all three components (Where, When and Size) mentioned above. This work, takes this direction and proposes for the first time a solution to the assessment of landslide hazard in a given area by jointly modeling landslide occurrences and their associated areal density per mapping unit, in space and time. To achieve this ambitious task, we have used a spatio-temporal landslide database generated for the Nepalese region affected by the Gorkha earthquake on the $25^{th}$ of April 2015. The model relies on a deep-learning architecture trained using an Ensemble Neural Network, where the landslide occurrences and densities are aggregated over a squared mapping unit of $1 \times 1$ km and classified/regressed against a nested 30 m lattice. At the nested level, we have expressed predisposing and triggering factors. As for the temporal units, we have used an approximately 6-month resolution depending on the mapped inventory dates. The results are promising as our model performs satisfactorily both in the classification (susceptibility) and regression (density prediction) tasks. We believe that the model we propose brings a level of novelty that has the potential to create a rift with respect to the common susceptibility literature, finally proposing an integrated framework for hazard modeling in a data-driven context.

To promote reproducibility and repeatability of the analyses in this work, we share data and codes in a github repository accessible from this link.

**Keywords:** Landslide Hazard; Deep Learning; Ensemble Neural Networks; Hierarchical models; Joint landslide occurrence and areal prediction; Spatio-temporal modeling.

[1]University of Twente, Faculty of Geo-Information Science and Earth Observation (ITC), PO Box 217, Enschede, AE 7500, Netherlands

[2]Physical Science and Engineering (PSE) Division,
King Abdullah University of Science and Technology (KAUST), Thuwal 23955-6900, Saudi Arabia

[3]Statistics Program, Computer, Electrical and Mathematical Sciences and Engineering (CEMSE) Division,
King Abdullah University of Science and Technology (KAUST), Thuwal 23955-6900, Saudi Arabia

# 1 Introduction

The literature on physically-based models for landslides shows various solutions of how to estimate where landslides can occur, when they occur, and how they may evolve (e.g., Formetta et al., 2016; Bout et al., 2018). This framework allows one to describe the dynamics of a landslide from its initiation, propagation, and entrainment to the runout and deposition (e.g., Burton and Bathurst, 1998; Zhang et al., 2013). As a result, metrics such as the velocity, runout height, overall landslide area, and volume constitute standard outputs of such a modeling approach (see, van den Bout et al., 2021a,b). However, these models are often constrained to relatively small areas because of spatial data requirements on geotechnical parameters. This limitation has stimulated the geoscientific community to develop data-driven models instead. Which are much more versed to be extended over large regions because, rather than requiring specific geotechnical properties, they can rely on terrain attributes and remotely sensed data acting as geotechnical proxies (Van Westen et al., 2008; Frattini et al., 2010). However, in doing so, the geoscientific community has primarily taken a route directed almost exclusively towards assessing where landslides may occur while neglecting other important characterstics. This notion is commonly referred to as landslide susceptibility (Reichenbach et al., 2018; Titti et al., 2021). As for the lesser number of publications focused on estimating when or how frequently landslides may occur at a given location, the community has produced a number of near-real-time predictive landslide models for rainfall (Intrieri et al., 2012; Kirschbaum and Stanley, 2018; Ju et al., 2020) and seismic (Tanyaş et al., 2018; Nowicki Jessee et al., 2018) triggers. With regard to characteristics such as velocity, kinetic energy and runout, albeit fundamental to describe a potential landslide threat (Fell et al., 2008; Corominas et al., 2014), these are currently impossible to be data-driven-modeled because no observed dataset of landslide dynamics exists to support the modelling and predicting paradigm of an Artificial Intelligence (AI). Guzzetti et al. (1999) proposed to alternatively model landslide areas, which can be easily extracted from a polygonal inventory. Nevertheless, the first spatially-explicit model able to estimate landslide areas has only been recently proposed by Lombardo et al. (2021). In their work, the authors exclusively estimated the potential landslide size at a given location, without informing whether the given location would have been susceptible in the first place. This limitation has been further addressed by Bryce et al. (2022) and Aguilera et al. (2022), implementing models that couple susceptibility and landslide area prediction together. Nevertheless, even in these cases, the absence of the temporal dimension in their work implies that no current data-driven model has even been capable to solve the landslide hazard definition (Guzzetti et al., 1999), jointly estimating where, when (or how frequently) and how large landslides may be in a given spatio-temporal domain.

The present work expands on the data-driven literature summarized above by proposing a space-time deep-learning model based on an Ensemble Neural Network (ENN) architecture. Neural Networks (NN) are not new to the landslide literature, though they have found the spotlight so far almost exclusively for automated landslide detection (Catani, 2021; Meena et al., 2022) and on to a lesser extent for landslide susceptibility assessment (Lee et al., 2004; Catani et al., 2005). Here, the main difference is that our ENN is built as an ensemble made of two elements, i.e., a landslide susceptibility classifier and a landslide density area regression model, both simultaneously defined over the same space-and-time domain. Thanks to the open data repository of Kincey et al. (2021), we were able to test our space-time ENN and to fully comply for the first time with the landslide hazard definition (as per Guzzetti et al., 1999).

The manuscript is organized as follows: Section 2 describes the data we used; Section 3 summarizes how we partitioned the study area; Section 4 lists the predictors we chose; Section 5 details our space-time ENN architecture; Section 6 reports our results, which are then discussed in Section 7, and Section 8 concludes our contribution with an overall summary and future plans.

# 2 Study area and landslide inventory

The 2015 Gorkha (Nepal) Earthquake is one of the strongest recent earthquakes in south Asia and specifically along the Himalayan sector (e.g., Kargel et al., 2016). The Mw 7.8 mainshock occurred on $25^{th}$ April 2015 and together with a sequence of aftershocks it was responsible for triggering more than 25,000 landslides (Roback et al., 2018). The ground motion did not only affect the Nepalese terrain right after the earthquake by co-siesmic landslides, but its disturbance increased the landslide susceptibility in the following years, a phenomenon commonly referred to as earthquake legacy (Tanyaş et al., 2021). The legacy of the Gorkha earthquake has been recently demonstrated by mapping a multi-temporal inventory, which has been publicly shared by Kincey et al. (2021). The authors mapped landslides across the area shown in Figure 1 from 2014 to 2018, including the co-seismic phase, as well as all pre-monsoons and post-monsoons seasons, with an approximate temporal coverage of six months. They used time series of freely available medium-resolution satellite imagery (Landsat-8 and Sentinel-2) and aggregated the resulting landslide areas at the level of a 1 km squared lattice. Overall, they mapped three pre-seismic and seven post-seismic landslide inventories in addition to the co-seismic one. Out of these, in this work we excluded three pre-seismic inventories and selected the inventories from April 2015 onward, because the effect of the ground motion and its legacy effect is present only after the event.. As a result, from the gridded database by Kincey et al. (2021), we extracted a total of eight landslide inventories.

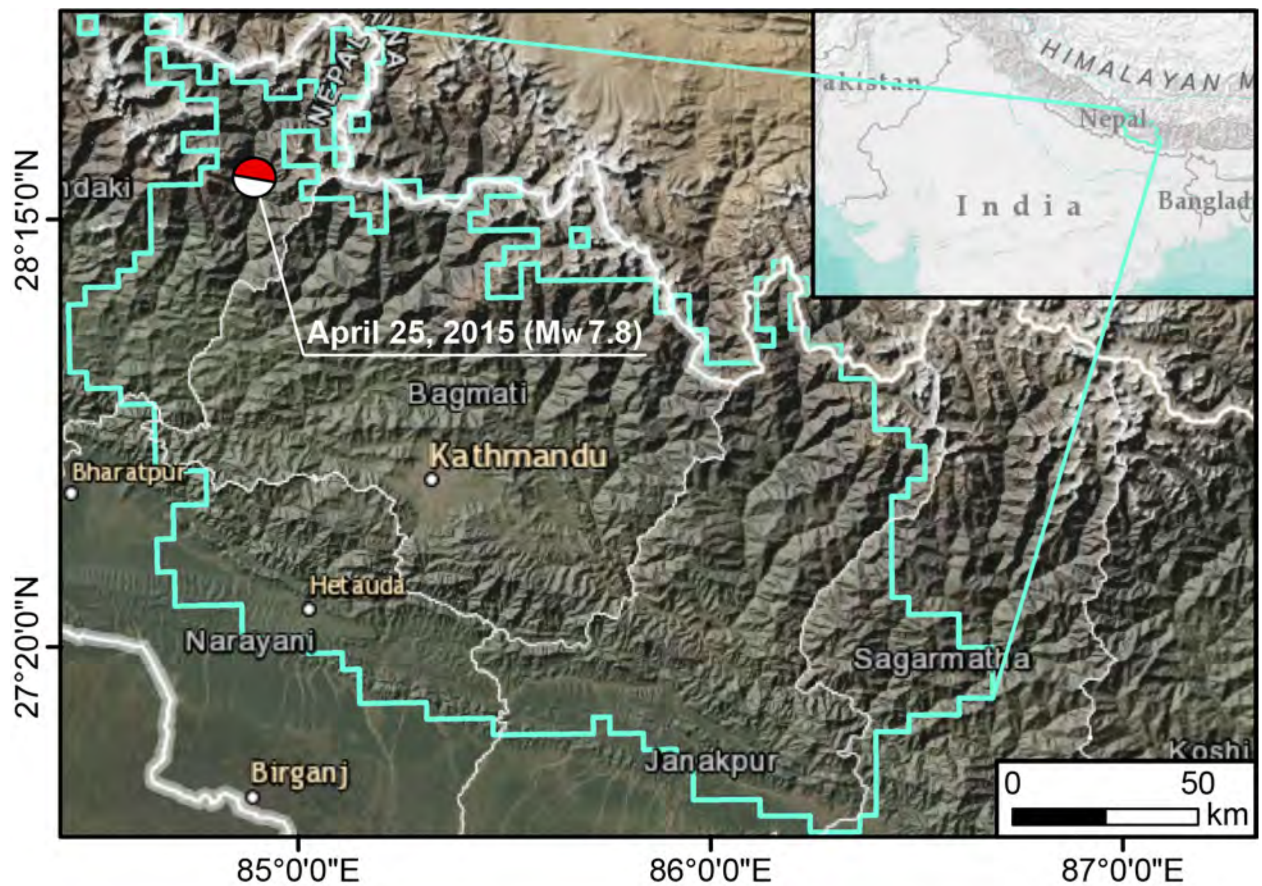


Figure 1: Study area defined within the cyan polygon, where Kincey et al. (2021) mapped the multitemporal landslide inventories upon which we based the analysis in this work. The Beach Ball shows the moment tensor of the energy release from 2015 Gorkha Earthquake.

It is important to stress that since the landslide information was aggregated at a 1 km resolution, it is not possible to disentangle single landslides, one from the others. In fact, each 1 km grid reports the whole landslide area mapped by the authors each time, without excluding the footprint of previous failures. For this reason, we had to include a pre-processing step where each temporal replicate has been re-calculated and re-assigned with the difference in landslide area density between two original subsequent inventories. In the attempt of focusing on newly activated landslides, we have then considered only grid cells with an increase in landslide area. The interpretation here is that an increase with time implies either newly formed landslides or re-activated ones. Conversely, the grids where the landslide area diminished with respect to their previous counterpart were assigned with a zero value under the assumption that there no landslide took place but vegetation recovery was instead responsible for the estimated change. The resulting temporal inventory at different time period over the 1 km grid is shown in Figure 2.

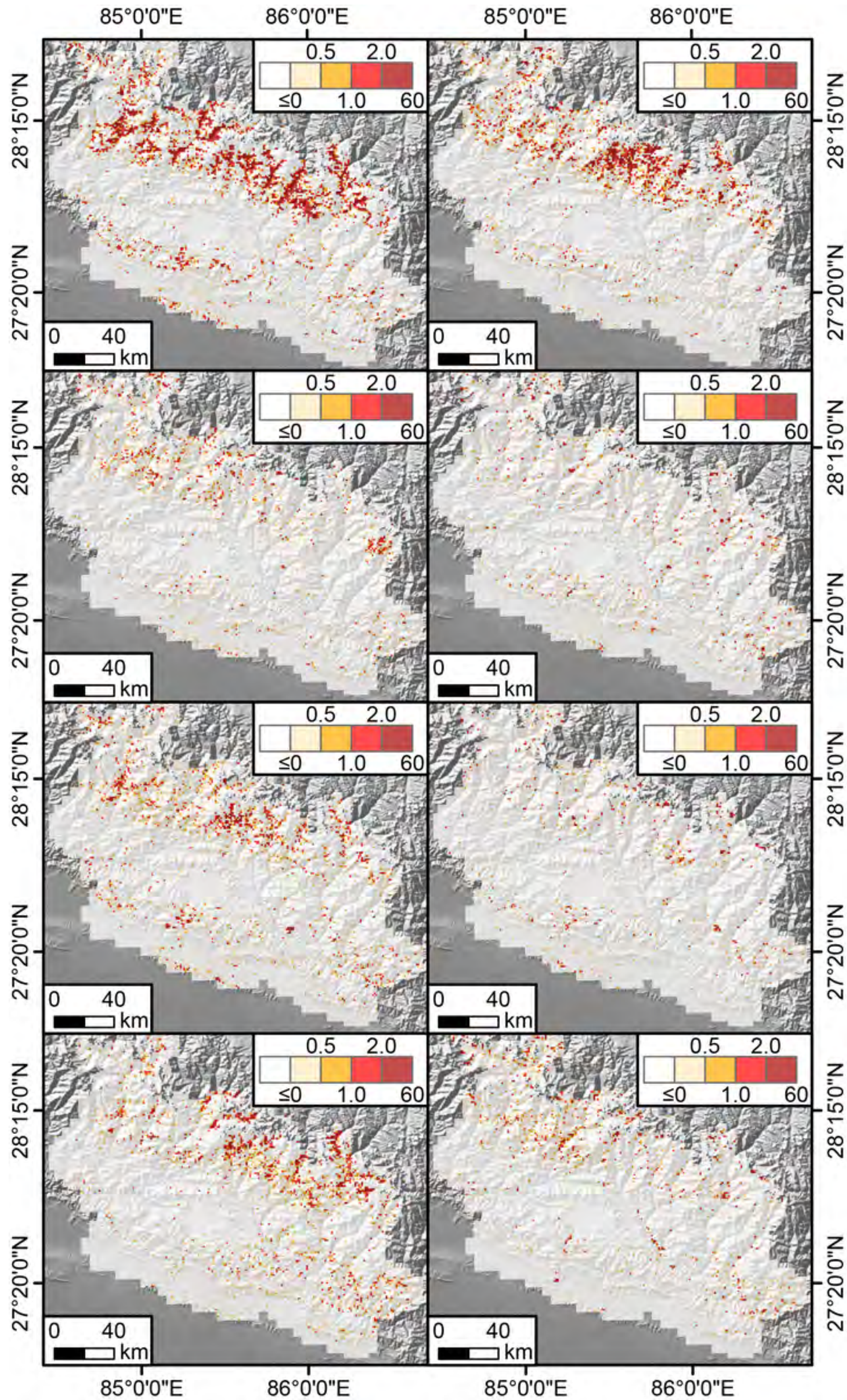


Figure 2: Landslide Area Density (% in a 1 km$^2$ grid) calculated as the difference between two consecutive inventories mapped with different time range provided by Kincey et al. (2021).

# 3 Selection of mapping units

To partition our study area, we use the same mapping unit defined by Kincey et al. (2021). Because the authors aggregated the landslide information on a $1 \times 1$ km$^2$ square grid, our model targets are defined within the same lattice structure. As for the definition of the predictor set, unlike current data-driven practices where medium resolution mapping units are assigned with the mean and standard deviation of the predictors under consideration (Lombardo et al., 2021), here we exploit the NN structure to treat each predictor as an image. In other words, each $1 \times 1$ km$^2$ square grid was not summarized with its mean and standard deviation values but the whole information expressed by small image patches which entered into our model.

Only feeding a single grid structure to the NN would neglect any spatial dependence coming from neighboring areas. Since, landslides are dynamic phenomena, it is therefore essential to inform the model about how the landslide distribution changes across the neighboring landscape, as well as the characteristics of the neighborhood under consideration. To do so, we extended the spatial vision of our ENN by creating two additional sets of lattices, each encompassing sixteen 1 km grids, in a $4 \times 4$ patch. Figure 3 further explains the mapping unit structures, wherein in panel (a) we can observe that the 1 km red polygonal lattice created by Kincey et al. (2021) contains $32 \times 32$ pixels of the underlying terrain characteristics. The subplot (b) shows how each patch is generated though the green boxes, containing 16 inventory grids. Each box will later be used as the training patches in the ENN, which in turn implies a $128 \times 128$ pixels structure (32 pixels $\times 4 = 128$) as input data. The model will then output 16 inventory grids, following the same data structure expressed at the $4 \times 4$ patch level. The reason to do so, is to also introduce spatial dependency in the model. Notably, if we would have used the single patch arrangement shown in Figure 3b, then the landscape characteristics along the edges of each patch would have been lost.

To account for this issue, we also produced a second patch arrangement, identical to the first but shifted by two kilometers in east and two kilometers in south. This operation returned the blue patches shown in Figure 3c. In this way, the total data volume is also increased providing multiple terrain and landslide scenarios defined over the different spatial data structures.

Note that these spatial manipulation procedures are quite common for Convolutional Neural Networks (e.g., Amit and Aoki, 2017). Here, we have simply adapted them in the context of the gridded structure defined by Kincey et al. (2021).

# 4 Predictors

The predictor set we chose features a number of terrain attributes, as well as hydrological and seismic factors. Those predictors are selected based on their influence on landslides which is observed by many existing works as represented in the table 1. Our assumption is that

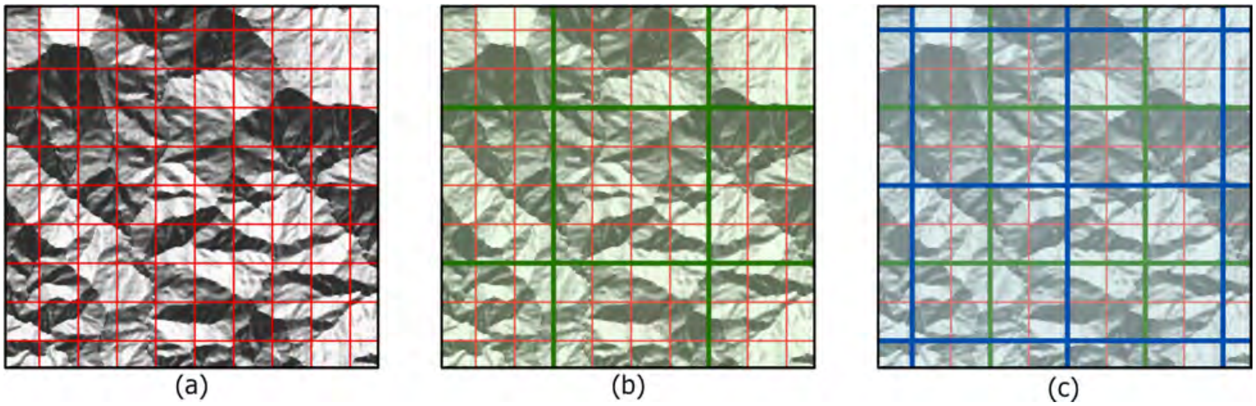


Figure 3: Panels showing the various mapping units structures: *(a)* the covariate and existing inventory grid structure, with 1 × 1 km. grid with 32 × 32 pixels of terrian image in the background *(b)* the patching of 4x4 inventory grid with 4 × 4 km. grid and *(c)* the shifted patch structure with similar grid structure as *(b)*.

their combined information is able to explain the distribution of landslide occurrences and area densities (the combined targets of our ENN) both in space and time. These predictors are listed in Table 1, graphically shown in Figure 4 and below we report a brief explanation to justify their choice.

Table 1: Predictors' summary

| Type | Covariate: Acronym \| Unit | Reference |
|---|---|---|
| Morphometric (30 m SRTM) | *Slope (Slope \| degrees)* | (Zevenbergen and Thorne, 1987) |
| Morphometric (30 m SRTM) | *Elevation (Elevation \| meters)* | – |
| Morphometric (30 m SRTM) | *Northness (Northness \| unitless)* | (Lombardo et al., 2018) |
| Morphometric (30 m SRTM) | *Eastness (Eastness \| unitless)* | (Lombardo et al., 2018) |
| Morphometric (30 m SRTM) | *Profile Curvature (PRC \| $m^{-1}$)* | (Heerdegen and Beran, 1982) |
| Morphometric (30 m SRTM) | *Planar Curvature (PLC \| $m^{-1}$)* | (Heerdegen and Beran, 1982) |
| Morphometric (30 m SRTM) | *Topographic Wetness Index (TWI \| unitless)* | (Sörensen et al., 2006) |
| Precipitation (∼5km CHRIPS) | *Maximum daily rainfall (Max. Precip.\| mm/day)* | (Funk et al., 2015) |
| Precipitation (∼5km CHRIPS) | *95% CI rainfall in the inventory period (95% CI Precip. \| mm/day)* | (Funk et al., 2015) |
| Seismic shaking (1 km USGS) | *Maximum Peak Ground Acceleration from main event and major aftershock (Max PGA \| $m/s^2$)* | (Worden and Wald, 2016) |
| Seismic shaking (1 km USGS) | *St. Dev. Peak Ground Acceleration (1Std. PGA \| $m/s^2$)* | (Worden and Wald, 2016) |
| Distance to River | *Distance to River (Dist2Riv \| meters)* | – |
| Monsoons after Earthquake (count) | *Monsoons after the Earthquake (Monsoons \| year)* | – |

The *Slope* carries the signal of the gravitational pull acting on potentially unstable materials hanging along the topographic profile (Taylor, 1948). *Elevation*, *Eastness* and *Northness* are common proxies for a series of processes such as moisture, vegetation and temperature (Clinton, 2003) and their effect on slope stability (Neaupane and Piantanakulchai, 2006;

Whiteley et al., 2019; Loche et al., 2022). As for the *Planar* and *Profile Curvatures*, these are known to control the convergence and divergence of overland flows (Ohlmacher, 2007). This hydrological information is also supported by *Topographic Wetness Index* and *Distance to River* (Yesilnacar and Topal, 2005). To these finely represented predictors, we also added a number of coarser ones, representing the potential triggers behind a landslide genetic process namely, *Rainfall* (both as its Maximum value and 95% Confidence Interval (CI) calculated from daily CHIRPS data spanning between two subsequent landslide inventories; Funk et al., 2015) and *Peak Ground Acceleration* (both as its Maximum value and standard deviation estimated for the Gorkha mainshock and the aftershocks available through the ShakeMap system of the United States Geological Survey (USGS); Worden and Wald, 2016). To these spatially and sometimes also temporally varying predictors, we also added a count of the number of monsoons after the Gorkha Earthquake to inform the model of potential legacy effects left by the ground shaking.

# 5 Neural networks

## 5.1 Model architecture

To contextually estimate landslide susceptibility and area density, we designed a NN with a multi-output design, relying on the same 1 km gridded data input. In short, the first model component estimates a "pseudo-probability" via a sigmoid function whereas the second component regresses the area density information against the same set of predictors used in the previous step.

The NN design is shown in the Figure 5. The susceptibility block is modified from the U-Net model (Ronneberger et al., 2015) with the backbone of Resent18 (He et al., 2015), where the model processes input information through the 18 blocks of Convolution, Batch Normalization (Ioffe and Szegedy, 2015), Rectified Linear Unit and Max pooling (Wu and Gu, 2015) with a total 23,556,931 number of trainable parameters which are variables that need to be optimized during the training process.

The decoder part consists of the U-Net structure, but unlike the conventional U-Net model, it produces an output scaled down by a factor of 8. The schematic design of the model is shown in Figure 6. To understand the spatial dependence between the different inventory grids ($1 \times 1$ km$^2$ grid), we have used a $4 \times 4$ aggregation patch as input for the susceptibility block, which is equivalent to $128 \times 128$ input pixels. After receiving $128 \times 128$ pixels, the convolution operation learns the contribution of physical properties such as earthquake and rainfall intensities as well as terrain characteristics to produce the susceptibility in a $4 \times 4 \times 1$ batch of $1 \times 1$ km$^2$ grids. We stress here that we specifically chose to use a $32 \times 32$ pixel structure per 1 km grid to convey all the possible information to the model and provide flexibility to the neural network to learn relevant information. As a result, the model can extract the relevant information it needs from the distribution of $32 \times 32$ pixels, rather than using arbitrary summary statistics such as the mean and standard deviation as

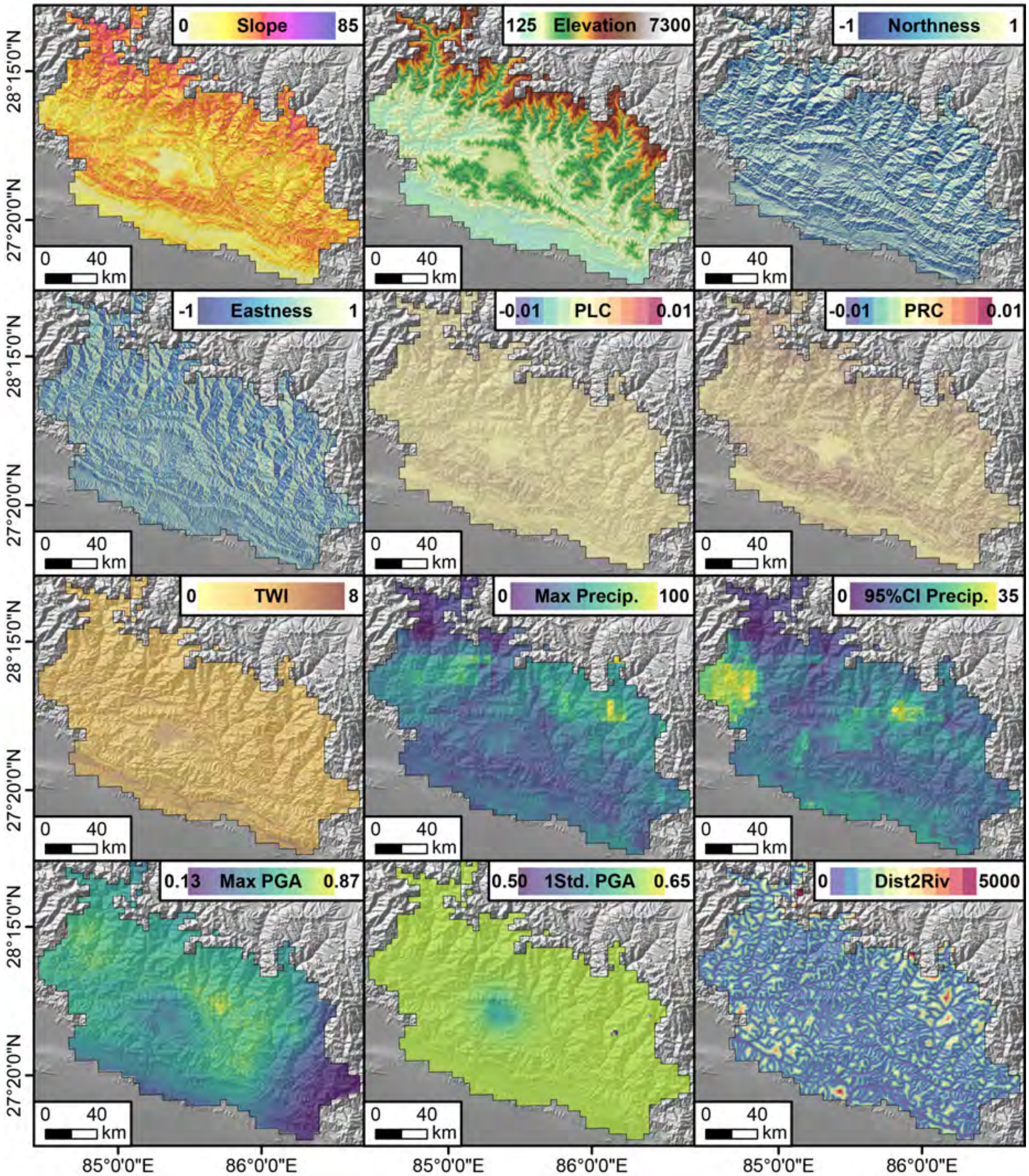


Figure 4: Predictors used for training the Ensemble Neural Network. The Max Precip. is one example of the maximum daily rain calculated for each of the inventories. The same applies to the 95% CI Precip. calculated as the difference between the 97.5 and 2.5 percentiles of the daily rainfall distribution. Max PGA and 1Std PGA are respectively the maximum and one standard deviation calculated from the peak ground acceleration maps of the main and after shocks. Dist2Riv is the Euclidean distance from each 30m pixel to the nearest streamline. PLC, PRC and TWI are acronyms for Planar Curvature, Profile Curvature and Topographic Wetness Index.

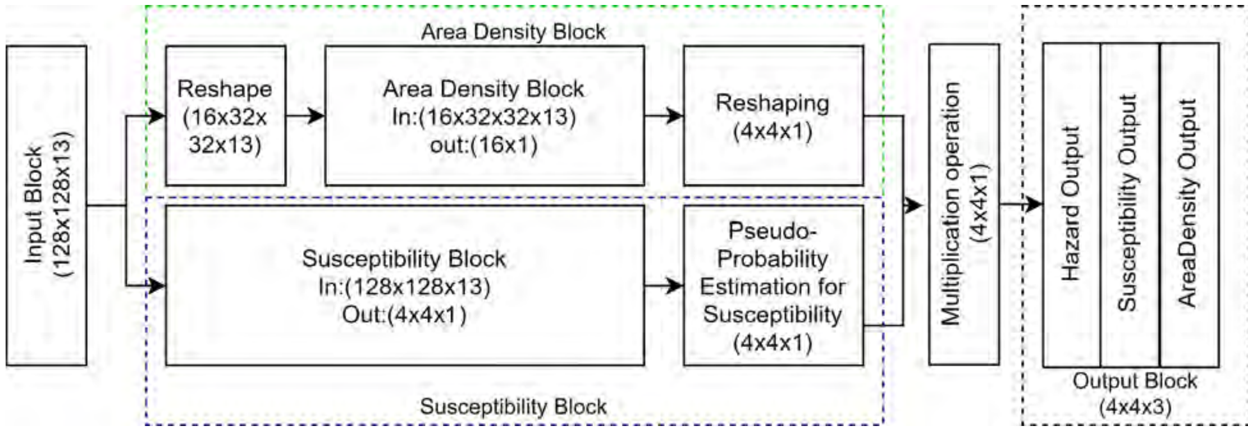


Figure 5: Designed landslide susceptibility and area density prediction model

per tradition in the geomorphological literature (e.g., Guzzetti et al., 2000; Lombardo and Tanyas, 2020). In other words, the model can learn by itself: (1) scanning $32 \times 32$ pixel images corresponding to single 1 km grid cells and (2) matching the image characteristics to the landslide presence/absence labels.

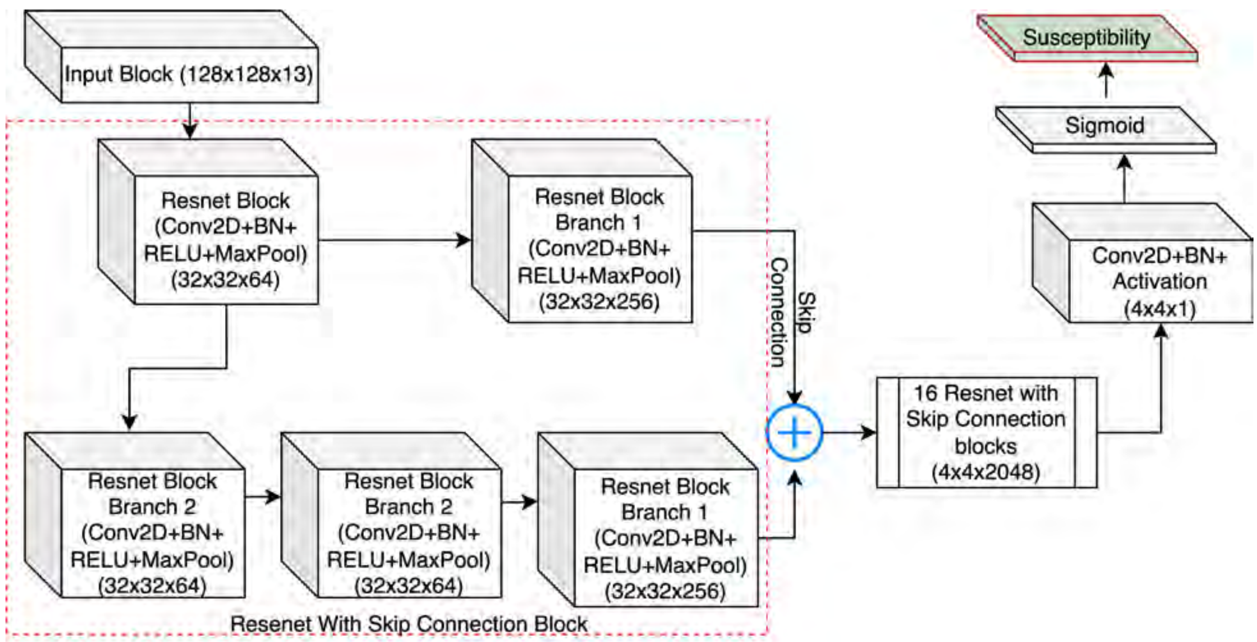


Figure 6: Susceptibility part of the model designed with U-Net like structure.

The area density block also relied on a 1 km grid structure but in this case, we did not introduce the $4 \times 4 \times 1$ neighborhood. Our choice is due to the fact that the landslide presence/absence data clearly reflect some degree of spatial dependence beyond the 1 km dimension and thus required for the model to be able to capture it. Conversely, the landslide area data does not present obvious clusters of small or large densities.

Furthermore, it is also evident that landslides are are discrete phenomena in space. This means that a large area density can be estimated at a 1 km grid but its neighbor may have not suffered from slope failures (area density = 0). Conveying this "salt and pepper" spatial structure into a U-Net architecture (via a $4 \times 4$ neighboring window) tasked with regressing continuous data, actually produces negative effects on the model (unreported tests).

To addres this issue, we reshaped the input data to a $16 \times 32 \times 32 \times 13$ shape, where 16 inventory grids, each associated with 13 predictors of $32 \times 32$ pixel size are present. The area density block is made of six dense sub-blocks, encompassing fully connected, batch normalisation (Ioffe and Szegedy, 2015) and dropout layers (Srivastava et al., 2014). Before passing the data to the dense block, we added one Convolution block consisting of Convolution, Batch Normalization(Ioffe and Szegedy, 2015) as well as Rectified Linear Unit and Max pooling (Wu and Gu, 2015) layer sto extract the features from the input patches. Once both the area density and the susceptibility are estimated, the area density needs to be reshaped to match the data structure of the susceptibility component. To then generate landslide hazard estimates, as per the definition proposed by Guzzetti et al. (1999), we added a step where the pseudo-probability of landslide occurrence is multiplied with the landslide area density, and finally output the landslide hazard together with the susceptibility and area density.

## 5.2 Experimental setup

To train the model, we used the Adam optimiser (Kingma and Ba, 2014), with an initial learning rate of $1e^{-3}$, exponentially decreasing every 1000 steps of training. Because simultaneously training a model with two outputs based on a large and complex dataset would be extremely difficult to achieve, we opted to train the two elements separately in the begining and combine their weights at the end of the learning process to generate a single model. Which is then further trained for few more steps to optimize the area density component for the non-landslide grids.

Binary classifiers are quite standard in machine/deep learning, thus for the susceptibility component we opted for a focal Traversky loss function ($FTL_c$, see equation below for clarity), as Abraham and Khan (2018) have shown this measure to be particularly suited for imbalanced binary datasets such as ours. The definition of Focal Traversky Loss is:

$$
\begin{aligned}
FTL_c &= \sum_c (1 - TI_c)^{\frac{1}{\gamma}}, \\
TI_c &= \frac{\sum_{i=1}^{N} p_{ic} g_{ic} + \epsilon}{\sum_{i=1}^{N} p_{ic} g_{ic} + \alpha \sum_{i=1}^{N} p_{ic} g_{ic} + \beta \sum_{i=1}^{N} p_{ic} g_{i\bar{c}} + \epsilon},
\end{aligned}
\tag{1}
$$

where, $\gamma$ is focal parameter, $p_{ic}$ is the probability that the pixel $i$ is of the lesion class $c$ and $p_{i\bar{c}}$ is the probability that the pixel $i$ is of the non-lesion class $\bar{c}$. The same holds for $g_{ic}$ and $g_{i\bar{c}}$. $\alpha$, and $\beta$ are the hyperparameters which can penalize false positives and false negatives and $\epsilon$ value was set to $1^{-}7$. Furthermore, $c$ is the class which in our case is 1 but in case of multi-class classification problems it can be any natural numbers. $FTL_c$ is the Focal Traversky Loss for binary classification problem and the $TI_c$ is the Traversky Index.

To train the susceptibility part of the model, we trained a standard U-Net equipped with an early stopping functionality for a total of 500 epochs. The stopping criterion was set to the detection of overfit that may last for over 10 epochs. The overall data was then randomly split into a training and testing sets to monitor the U-Net learning process.

As for the area density component, we opted for a loss function expressed in terms of mean absolute error ($MAE$, see equation below for clarity), following the recommendations in Qi et al. (2020). The definition of the MAE is:

$$\text{MAE} = \frac{\sum_{i=1}^{n} |y_i - \hat{y}_i|}{n} \tag{2}$$

where, $y_i$ is the observed area density and the $\hat{y}_i$ is predicted area density in the $i - th$ pixel and n is total number of samples in one batch.

To train the area density part of the model, the imbalance in zeros and ones hindered the optimisation process because the mean absolute error function did not perform well with the imbalanced data. This led to exploding gradients, and the model produced all zero outputs. To solve this issue, we gradually increased the complexity of the task by subsampling the data and transforming the distribution of area density. The process is commonly known as curriculum learning (Wang et al., 2021) which lets the model learn a simple task at the start, and the process continues by gradually increasing the complexity of the subsequent tasks, each one linked to the previous one. To do so, we first removed all data points which contained zeros among the area density 1 km grids and then we log-transformed the target variable to convert the exponential-like distribution to a gaussian like distribution. Once the data was expressed according to a near-normal distribution, we trained the model for 200 epochs including an early stopping criterion. Then, we used the estimated parameters to initialize the subsequent steps. Specifically, with initialisation parameters available, we removed the log transformation and trained the model directly in the original landslide area density scale. This step was further run over 200 epochs and the resulting parameters were fine-tuned to match the overall landslide area density distribution; i.e., this time also featuring the 1 km grids with zero density. The data were then randomly divided into 70% for calibration and 30% for validation routines.

## 5.3 Performance metrics

We used the following performance metrics for susceptibility and the area density components.

### 5.3.1 Susceptibility component

To evaluate the model's performance during the training process and the inference, we used two common metrics, namely the F1 score (Nava et al., 2022) and the Intersection over

Union (IOU) score (e.g., Huang et al., 2019). We did not use binary accuracy because it is heavily influenced by data imbalance (Li et al., 2022) and can produce high accuracy, even for poor classifications. The F1 score (3) calculation is calculated as:

$$\begin{gathered}F1=\frac{2\times \text{ precision } \times \text{ recall}}{\text{precision } + \text{ recall}}, \\ \text{precision } =\frac{TP}{TP+FP}, \text{ recall } =\frac{TP}{TP+FN},\end{gathered} \tag{3}$$

where, TP denotes the True Positive, FP denotes the False Positive, TN denotes True Negative and FN denotes the False Negative in the confusion matrix.

As for the IOU, this is another common metric for binary classifiers and it may be computed as:

$$IOU=\frac{TP}{TP+FN+FP}, \tag{4}$$

where, TP denotes the True Positive, FP denotes the False Positive, TN denotes True Negative and FN denotes the False Negative in the confusion matrix.

We chose to use the IOU because it is a metric specifically dedicated to highlight the accuracy in predicting the number of susceptible pixels and their location in a raster image (Monaco et al., 2020). Furthermore, to visualize how the model performs at different probability thresholds and what is the performance capacity of the model we also evaluated the Receiver Operating Characteristic (ROC) (Fawcett, 2006) curve which is generated from the True Positive Rate and False Positive Rate. Moreover, we calculated the Area Under the Curve (AUC) of the ROC curve to evaluate the model's performance and to observe if the model overfits.

### 5.3.2 Area density component

To evaluate the training process for the landslide area density, we opted to use the MAE from 5to monitor how the algorithm converges to its best solution minimising such parameter. During the inference process, we also considered the Pearson's R coefficient Pearson (1895) defined as:

$$\begin{aligned}R&=\frac{\sum\left(x_i-\overline{x}\right)\left(y_i-\overline{y}\right)}{\sqrt{\sum\left(x_i-\overline{x}\right)^2\sum\left(y_i-\overline{y}\right)^2}}, \\ where&, \\ R&=\text{ correlation coefficient },\\ x_i&=\text{ values of the } x\text{-variable in a sample },\\ \overline{x}&=\text{ mean of the values of the } x\text{-variable },\\ y_i&=\text{ values of the } y\text{-variable in a sample },\\ \overline{y}&=\text{mean of the values of the } y\text{-variable}\end{aligned} \tag{5}$$

This parameter essentially provides the degree of correlation between two datasets, i.e., the observed and predicted landslide density per 1 km grid. A perfect model should have Pearson's R-value of 1, whereas two totally uncorrelated vectors would return a Pearson's R-value of 0.

# 6 Results

This section reports the model performance, initially from a pure numerical perspective. Later we will translate this information back into maps and their repeated temporal characteristics.

Figure 7 offers an overview of the performance our ENN returned for its two components. The left panel reports an AUC of 0.93, associated with a F1 Score of 0.96 and IOU of 0.95. This predictive performance complies with the classification performance of other data-driven models. This is very normal because NNs as much as other machine/deep learning tools and advanced statistical methods have proven to be able to reliably classify a landscape into landslide prone/unstable slopes (e.g., Lombardo et al., 2019; Steger et al., 2021). Traditionally, the only missing element is that the vast majority of efforts so far have been spent solely in the context of a pure spatial predictions whereas the temporal dimension has been explored in a very limited number of cases (Samia et al., 2017; Lombardo et al., 2020). Conversely, the performance of the area density component are far beyond the few analogous examples in the literature. So far, no spatially nor temporally explicit model exists for landslide area density. However, four recent articles have explored the capacity of predicting landslide areas (Lombardo et al., 2021; Aguilera et al., 2022; Bryce et al., 2022; Moreno et al., 2022). All of them have returned suitable predictive performance, but still far from the match seen in the second panel of Figure 7, between observed and predicted landslide density. There, an outstanding alignment along the 45 degree line is clearly visible, together with a Pearson's R coefficient of 0.93 and a MAE of 0.26%. It is important to stress that such metrics are calculated including the 1 km grids with zero landslide densities, i.e., the validation set in the study area as a whole. We also computed the same metrics exclusively at grid cells with a positive density, these resulting in a Pearson's R coefficient of 0.92 and a MAE of 0.24%

With a closer look, though we can note a few exceptions, with some observations being strongly underestimated and very few cases being overestimated. Which might be because we used MAE as the loss function and because it is based on the mean, underestimation of smaller values in the batch does not generate the high MAE and the model is optimized by minimization, so, it puts more focus on the large landslides causing underestimation of the smaller values. This problem could also have been influenced due to log-transformation of the data in the beginning of the training process which converted smaller values to very small which did not had much influence in the loss function causing bad prediction on those regions.

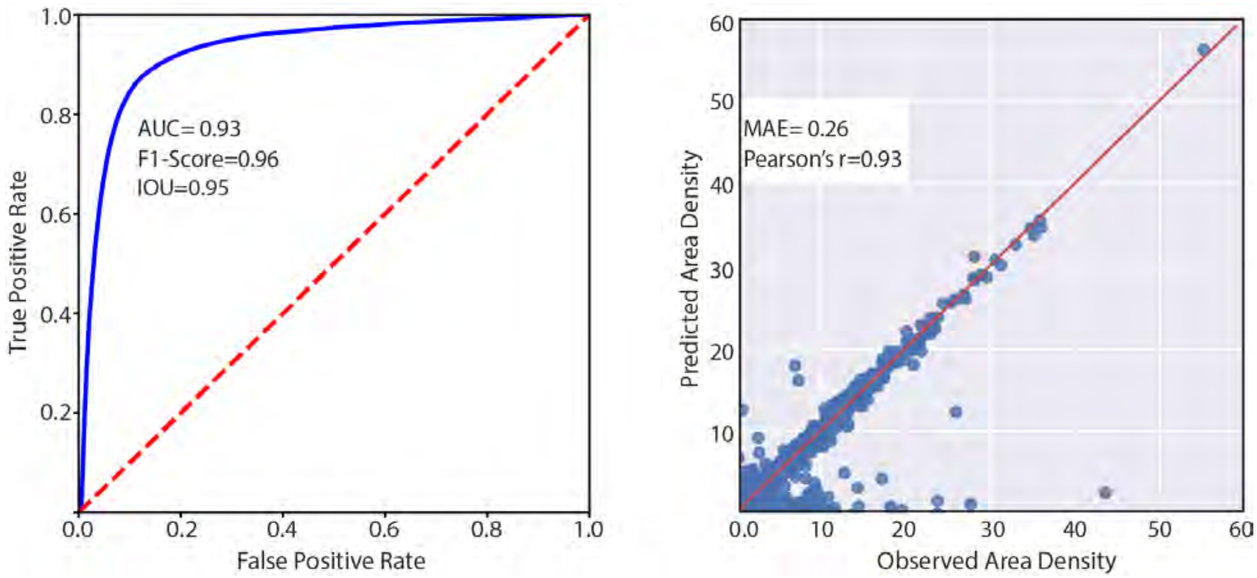

Figure 7: Summary of model's performance for the two components: landslide susceptibility in the left panel and Area Density in the right panel in the validation data.

These two plots offer a graphical overview of our ENN performance but they do not convey their signal in space and time. To offer a geographic and temporal overview of the same information, we opted to translate the match between observed and predicted values into maps, both for the susceptibility and area density components. Figure 8 shows confusion maps (Titti et al., 2022; Prakash et al., 2021), where the distribution of TP, TN, FP, FN is geographically presented for the coseismic susceptibility as well as the following seven post-seismic scenarios. Across the whole sequence of maps, what stands out the most is that the TP and TN largely dominate the landscape, with few local exceptions. Notably, aside from the geographic translation of the confusion matrix, we reported the actual counts in logarithmic scale through the nested subpanels. There, the dominant number of TP and TN is confirmed once more and a better insight is provided on the model misses (FP and FN).

Figure 9 highlights the mismatch between observed and predicted landslide area densities. Most of the residuals are confined between -1 and +1 percent, with a negligible number of exceptions reaching an overestimation of -45% and an underestimation of +15%. Aside from these outliers, the most interesting element that stands out among these maps is the fact that the residuals do not exhibit any spatial pattern. They actually appear to be distributed randomly both in space and time.

Having stressed the predictive performance reached by our ENN, in Figure 10, we finally offer a direct overview of the two outcomes (susceptibility and area density) as well as their product (hazard). Notably, Figure 10 reports the co-seismic case only and the post-monsoon estimates. We opted for this for reasons of practicality and visibility in a quite crowded subpaneled figure. To accommodate for the potential curiosity of the readers, we recall here that code and data are open and accessible at this link.

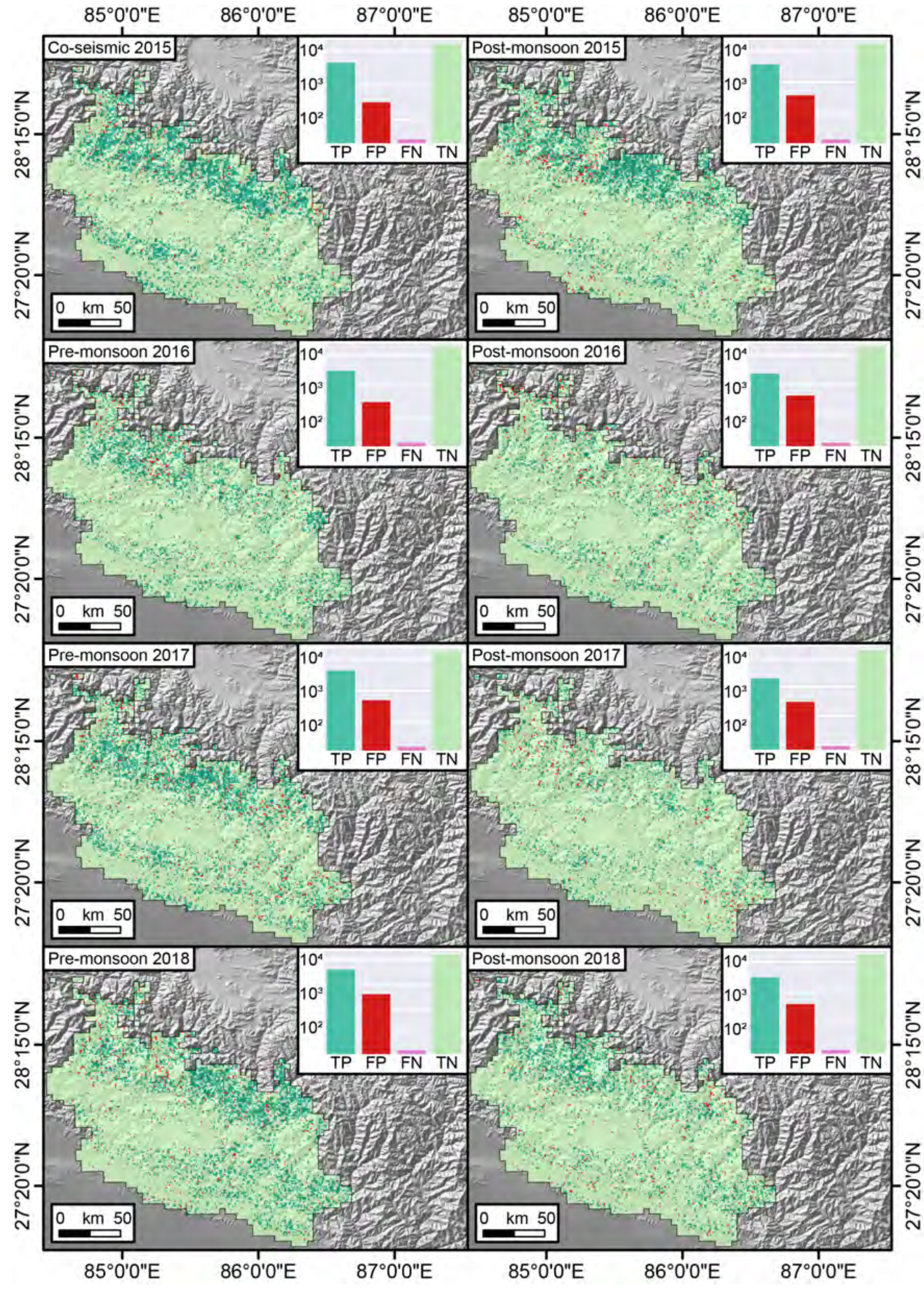


Figure 8: Confusion Maps offering a cartographic predictive of the performance for the susceptibility component. the TP, FP, FN and TN are represented in the log scale.

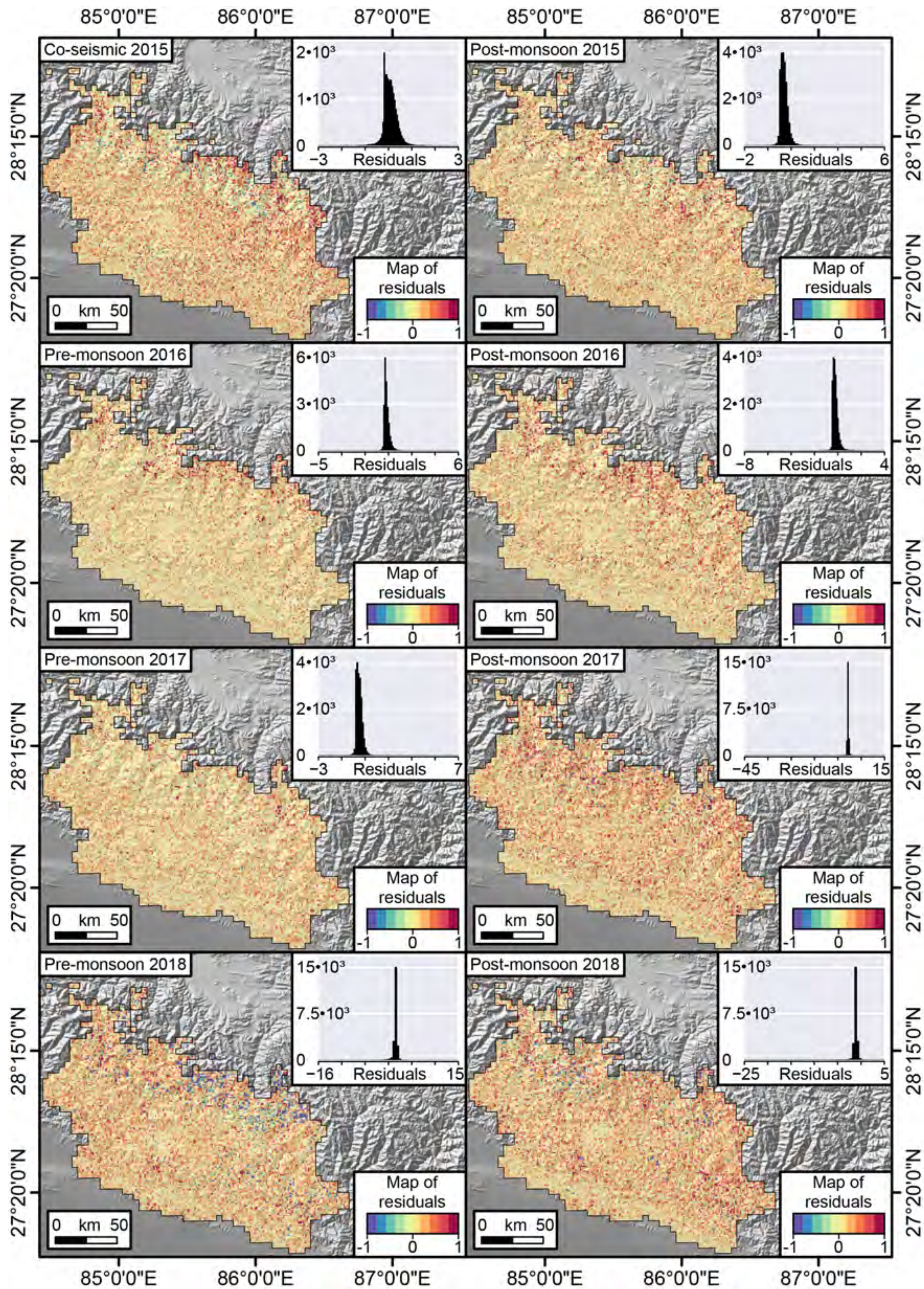


Figure 9: Maps displaying the pre- and post- monsoon residuals for the area density (expressed as percent). The residuals are computed as observed landslide density minus the corresponding predicted values.

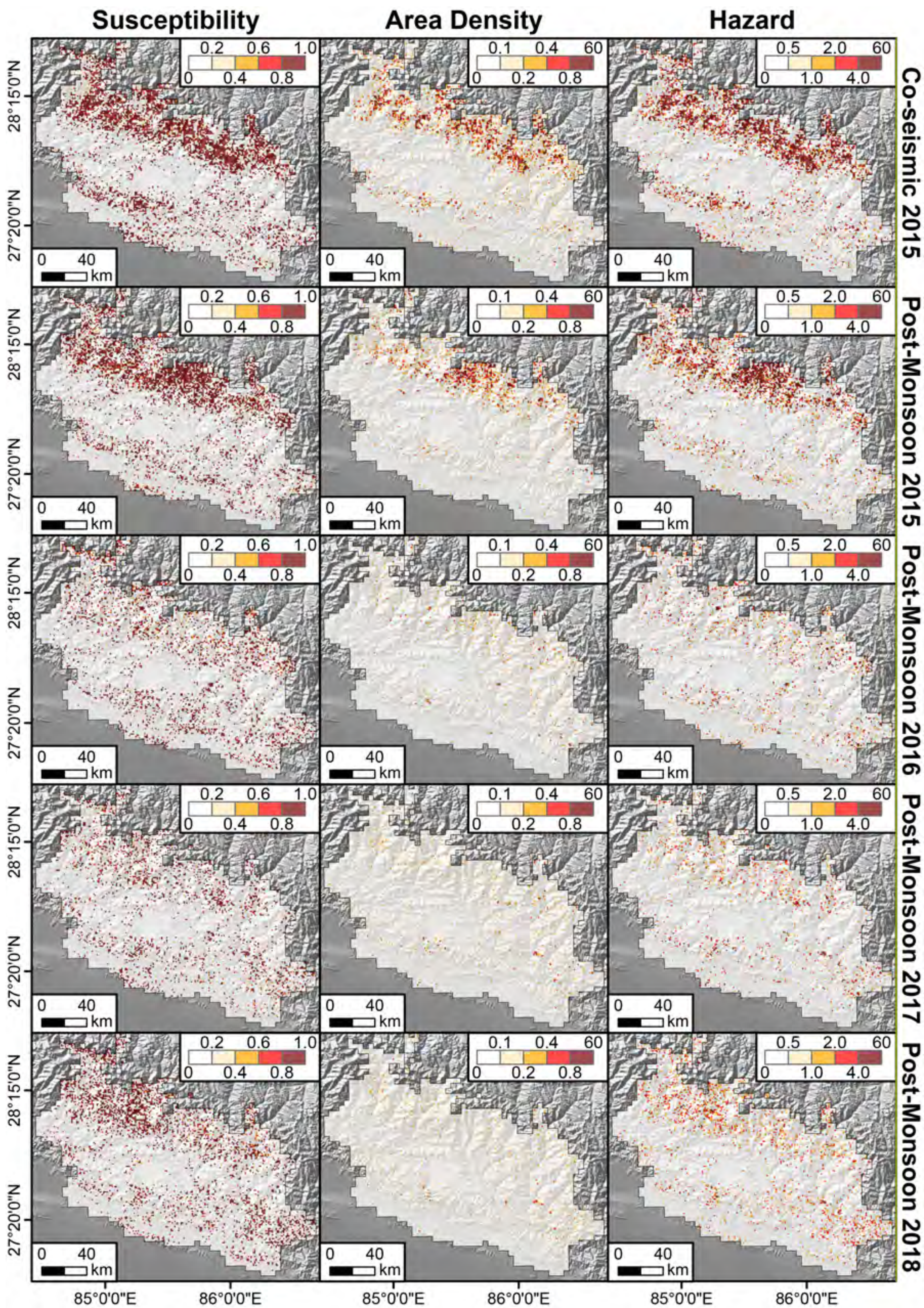


Figure 10: Predicted landslide susceptibility, area density and hazard over time for Post Monsoon seasons only, because those period had most of the landslide.

Reading these maps should be intuitive, but below we stress the assumptions behind the hazard one, being the first time such a map has ever been shown. The first column reports the probabilities of landslide occurrence per 1 km grid. The second column shows the predicted landslide area density for the same 1 km lattice. The product of the two delivers an important element, where only coinciding high susceptibility and high density grids stand out. The rational behind this is that large probability values of landslide occurrence will be inevitably canceled out whenever multiplied by low area density values. The same is valid in the opposite case. Large expected densities will be canceled out if multiplied by very low susceptibility values. Thus, the hazard maps really do inform of the level of threat one may incur at certain 1 km grids and certain times, because a high hazard value implies that the mapping unit under consideration is not only expected to be unstable but the resulting instability is expected to lead to a large failure, too.

The implications of the estimated patterns and considerations in terms of hazard will be further explored in Section 7. To support such discussions and highlight the link between susceptibility, hazard and their temporal evolution, we opted to plot their signal via two-dimensional density plots, these been shown in Figure 11.

We can observe an interesting element, attributable to a concept known as earthquake legacy in the geomorphological literature. In fact, high landslide area density values associated to high susceptibility conditions, are quite represented on the coseismic panel as well as the first post-seismic one. However, as time passes, the density and proneness of the landscape appears to be estimated with lower landslide susceptibilities and densities.

# 7 Discussion

In this section we discuss the model's performance, applicability, limitations and necessary future developments in two subsections containing the supporting and opposing arguments.

## 7.1 Supporting arguments

The model results and the observations show that the deep learning-based methods perform well in predicting the landslide susceptibility as well as area density through a joint modelling approach. Such models can obviously provide much more information than modelling only susceptibility (Lombardo et al., 2021). Only using the susceptibility information is blind to landslide characteristics such as how many landslides may manifest or how large they may become once they start moving downhill. Thus, the combined information of which slope may be considered unstable and the expectation on the landslide can become an important source of information not only for hazard assessment but even for risk reduction and management practitioners, once combined with potentially vulnerable elements.

Our ENN has shown the capacity to assess the two core elements and interesting considerations can be made on its outcome. Figure 8 shows that each inventory mostly produced True Positives and Negatives across the whole study site. More importantly, the number of

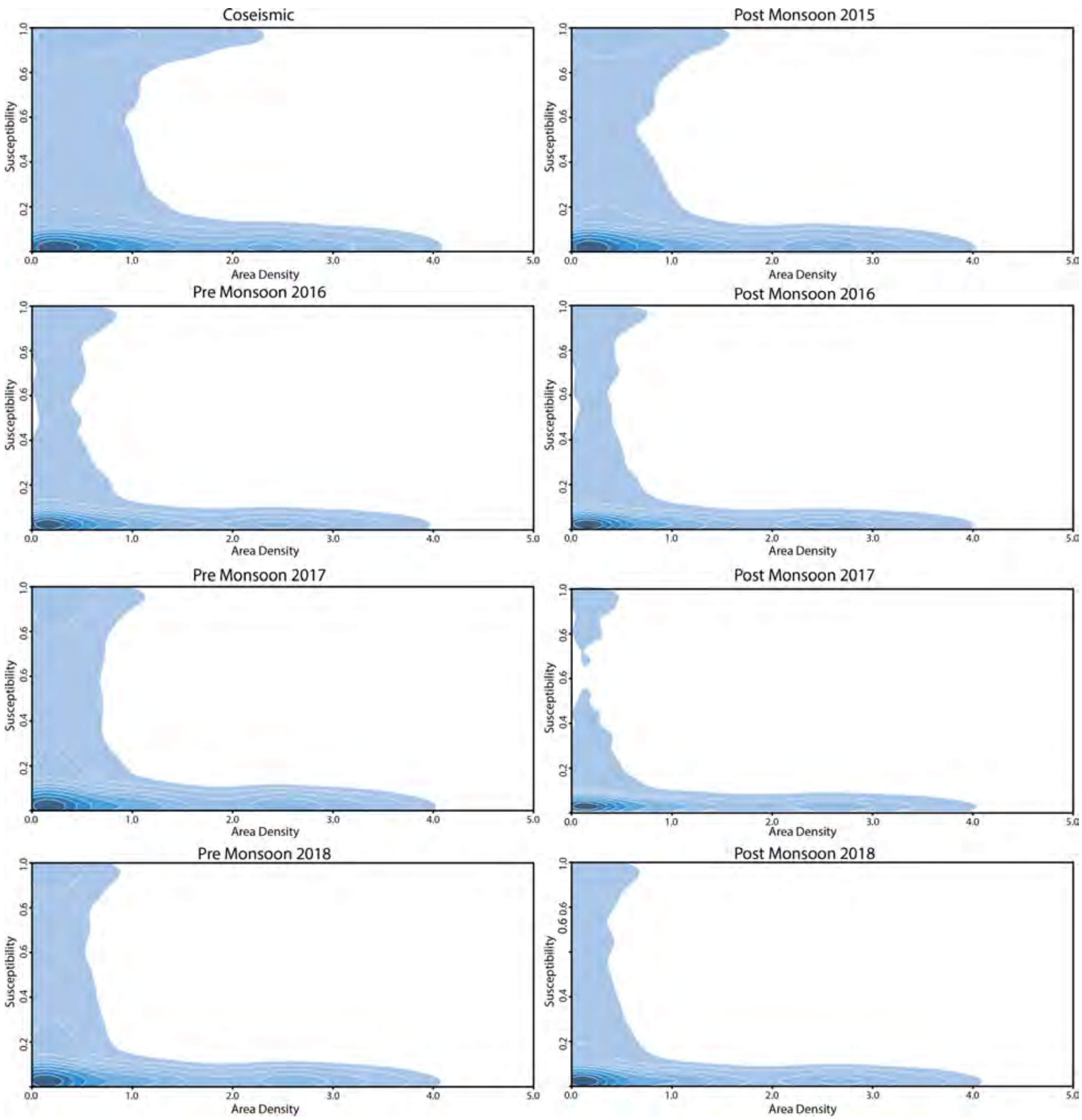


Figure 11: Contour plot of Area Density versus Susceptibility in different time periods showing how the area density and susceptibility are related to each other. Where, lighter color represents the lower desnity of the values and darker color represents the higher density of the values.. Furthermore, it shows how in different period after the earthquake the area density and susceptibility are distributed over space and how the range of susceptibility and area density changes.

False Negatives was so low to the point of being negligible. As for the False Positives, their number is reasonable and actually points out at locations where landslides did not take place in that particular moment but that may still generate slope failure in the future. As for the area component, Figure 9 shows that the patterns of the residuals appear quite random both in space and time, thus fulfilling the homoscedasticity requirements of our data-driven model. We can also stress that most of the residuals away from few percentage points are confined towards negative values. This implies that our model tends to overestimate the landslide area in a few isolated cases. However, similarly to the point raised for the FP in Figure 8, this outcome is to be expected. A negative residual indicates a location where the observed landslide area is lower than the predicted one. As most of the study site is characterized by grid cells where landslides did not occur, a negative residual points out at locations that may not have exhibited landslides in the first place, but whose geomorphological characteristics still indicate a likely release of a relatively larger unstable mass in the future.

Ultimately, Figure 10 shows the constructive and destructive interference between the susceptibility and area density signals. This leads to isolating landslide hazardous locations, which appear to be mostly located along the highest portions of the Himalayan range under consideration. There, a greater hazard is to be reasonably expected for the higher relief is associated with a higher gravitational potential and thus with a greater conversion into kinetic energy as the given landslide triggers, propagates and finally halts.

An interesting by-product of our ENN can be also seen in Figure 11. There, the high hazard levels estimated for the first two landslide inventories are shown to decay with time. This was also visible in the raw data shared by Kincey et al. (2021). Such a decay, supports the notion of earthquake legacy effects on landslide genetic processes, something still under debate in the geomorphological literature. In fact, our output could bring additional information on this topic supporting the scientific debate on landslide recovery (the time required for a given landscape to go back to pre-earthquake susceptibility conditions) by observing the predicted susceptibility change over time. Overall, multi-temporal landslide inventories and various associated parameters (e.g., number, size, area or volume of landslides) have already been used to explore landslide recovery in post-seismic periods (eg., Tanyas et al., 2021). However, this has usually been done at a very generic and broad scale, leaving the slope scale usually out of the analytical process. Therefore, we see an added value of our model as it provides a comprehensive evaluation of landslides occurrences and their size. Specifically, we could provide an even richer perspective on the earthquake legacy (or landslide recovery time) by assessing the spatio-temporal patterns of the landslide hazard rather than the susceptibility alone. It is worth noting that examining the landslide recovery is beyond the scope of this research. Yet, something worth to be shared with the readers is that the decay we observe appears to slow down in 2017 and 2018, with an actual slight increase in both the number of landslides, susceptibility, area density and hazard. During those years though, Kincey et al. (2021) could not regularly map landslides as they previously did. Thus, both pre-monsoon seasons in 2017 and 2018 were mapped on a longer time window compared to what the authors did in previous years, slightly inducing a temporal bias in the model.

Another element worth noting relates to the fact that landslides across any given landscape are rare events. Thus, the number of presences are always going to be much smaller than to the absences. This creates imbalanced data sets which are often not ideally modeled in the deep learning context (see, Johnson and Khoshgoftaar, 2019). In turn, imbalanced data sets limit the use of traditional metrics such as accuracy and the use of loss functions such as Binary Cross Entropy, because the latter will produce high number of false negatives. We addressed this problem by adopting a Focal Taversky loss for the susceptibility component (Abraham and Khan, 2018). As for the area density component, we also faced some technical issues. Overall, 85% of the 1 km grids cells had a zero density value assigned to them (no landslides). In addition to this issue, the area density distribution is quite positively skewed and regression tasks in deep learning have been mostly tested in the context of Gaussian or near-Gaussian distributions. To solve this problem, we had to split the modeling routine into a series of intermediate operations. First, we removed all zeros and used log transformation of the data to turn it into a normal distribution. From this, we trained the first stage of our area density component. Once the model converged to its best solution in the log-density domain, we interrupted the training procedure, removed the log transformation and further proceeded to train our model. This approach bypassed the need to implement even more complex NN architectures able to handle heavy tailed distributions typical of extreme value theory (Weng et al., 2018).

## 7.2 Opposing arguments

Even though the model produced outstanding results, there is still much room for improvement. As mentioned before, we addressed the heavy-tailed density distribution by making use of a log-transformation. Moreover, we used the L1 losses to measure the model convergence. These imply we used the negative log-likelihood of a normal distribution, which in turn inherently assume a normal distribution of the error. However, due to the fact that the area density follows an extreme value distribution in its tail region, instead of a model built on a log-transformation and then re-trained on the original density scale, a more straightforward procedure would directly use the original data distribution and make use of performance metrics or losses that are suitable for the considered data. However, due to lack of matured research on existing methods for using extreme value theory with deep learning, we could not use such approach. For the further research, for instance, one of the possible approaches could the integration of extreme value distributions (Davison and Huser, 2015) within our regression model. A similar procedure has been recently proposed to model wildfires (Richards et al., 2022) but in the case of quantile regression problem.

Moreover, our model relies on a gridded partition of the geographic space under consideration. This lattice has two main elements that call for further improvements. The first is related to the size of the lattice itself. A 1 km grid cell is quite far from the spatial partition required to support landslide-risk-reduction actions. Thus, the current model output can offer a far richer information compared to the sole occurrence probabilities. However, to be actually useful for territorial management practices, the scale at which we trained should be probably downscaled at a finer resolution. The second element where our ENN can be further improved in terms of spatial structure has to do with the geomorphological significance of a lattice when used to model landslides. Such geomorphological processes in fact, do not follow a regular gridded structure. In other words, when geomorphologists go to the field, they do not see grids, whether they are few centimeter or the 1 km scale of our model. What a geomorphologist sees is a landscape partitioned into slopes. Slopes are also the same unit geotechnical solutions aim to address. Thus, an improvement to our ENN could involve moving away from a gridded spatial partition and towards more geomorphological-oriented mapping units such as slope units (Alvioli et al., 2016; Tanyaş et al., 2022b), sub-catchments or catchments (Shou and Lin, 2020; Wang et al., 2022).

It is important to stress here that the structure of a Convolutional Neural Network mostly requires gridded input data. Thus, the extension towards irregular polygonal partitions such as the ones mentioned above would also require an adaptation of our ENN towards graph-based architectures (Scarselli et al., 2008).

Aside from the technical improvements we already envision, a key problem we could not address has to do with the lack of detailed spatio-temporal information on roadworks. Landscapes where roads are built may relapse through pronounced mass wasting (Tanyaş et al., 2022a). Nepal is known for small roads to be built without accounting for the required engineering solutions the maintain slope stability (McAdoo et al., 2018). Specifically, Rosser et al. (2021) point out that the elevated landslide susceptibility captured in post-seismic periods of the Gorkha earthquake could be partly associated with road construction projects. Thus, landslides trigger on steep slopes due to human interference, which we could not include in our model. During the very first phase of our model design, we actually tried to map those roads using freely available satellite images such as Sentinel 2 and PlanetScope. However, because the spatial resolution of those satellites is relatively coarse and the typical "self-made" roads are quite small (2-3 meters in width), we could not automatize the road-mapping procedure to match our ENN spatio-temporal requirements. Therefore, rather than conveying to the model wrong information, we opted for not introducing road-network data to begin with. This is certainly a point to be improved in the future, not only for the Nepalese landscape but for any mountainous terrain where anthropogenic influence may bias the spatio-temporal distribution of landslides.

Ultimately, we stress that the vast majority of Neural Networks are tailored towards solving prediction tasks and our ENN essentially offered the same extraordinary performances reported in many other deep learning applications. However, this architecture makes it very difficult to understand the causality behind the examined physical process. As our goal is to introduce the first unified spatio-temporal hazard model, causality may not be a fundamental requirement at this stage. However, we envision future efforts to be directed towards more interpretable and causal machine/deep learning.

# 8 Concluding remarks

The model we present is a data-driven model capable of estimating where and when landslides may occur, as well as the expected landslide area density per mapping unit. We achieved such a modeling task thanks to an Ensemble Neural Network architecture, a structure that has not found yet its expression within the geomorphological literature, hence, making this model first of its kind. The implications of such a model can be groundbreaking because no data-driven model has provided an analogous level of information so far. The predictive ability of the model we propose still needs to be explored isolating certain types of landslides, tectonic, climatic and geomorphological settings. If similar performance will be confirmed, then this can even open up to a completely different toolbox for decision makers to work with. So far, territorial management institutions rely almost exclusively on susceptibility maps in case of large regions and for long term planning. The dependency on the concept of landslide susceptibility is also valid for regional and global organizations providing near-real-time or early warning alerts for seismically or climatically triggered landslides. The model we propose can potentially link these two elements and provide an even richer information, exploiting its predictive power away from the six month time resolution we tested here and more towards near-real-time or daily responses for various scales applications.

We conclude stressing once more that we share data and codes in a github repository accessible at this link to promote reproducibility and repeatability of the analyses presented in this work.

# Acknowledgement

This article was supported by King Abdullah University of Science and Technology (KAUST) in Thuwal, Saudi Arabia, Grant URF/1/4338-01-01.

# References


Abraham, N. and Khan, N. M. (2018) A novel focal tversky loss function with improved attention u-net for lesion segmentation. CoRR **abs/1810.07842**.

Aguilera, Q., Lombardo, L., Tanyas, H. and Lipani, A. (2022) On The Prediction of Landslide Occurrences and Sizes via Hierarchical Neural Networks. Stochastic Environmental Research and Risk Assessment pp. 1–18.

Alvioli, M., Marchesini, I., Reichenbach, P., Rossi, M., Ardizzone, F., Fiorucci, F. and Guzzetti, F. (2016) Automatic delineation of geomorphological slope units with r.slopeunits v1.0 and their optimization for landslide susceptibility modeling. Geoscientific Model Development **9**(11), 3975–3991.

Amit, S. N. K. B. and Aoki, Y. (2017) Disaster detection from aerial imagery with convolutional neural network. In 2017 international electronics symposium on knowledge creation and intelligent computing (IES-KCIC), pp. 239–245.

van den Bout, B., van Asch, T., Hu, W., Tang, C. X., Mavrouli, O., Jetten, V. G. and van Westen, C. J. (2021a) Towards a model for structured mass movements: the OpenLISEM hazard model 2.0a. Geoscientific Model Development **14**(4), 1841–1864.

van den Bout, B., Lombardo, L., Chiyang, M., van Westen, C. and Jetten, V. (2021b) Physically-based catchment-scale prediction of slope failure volume and geometry. Engineering Geology **284**, 105942.

Bout, B., Lombardo, L., van Westen, C. and Jetten, V. (2018) Integration of two-phase solid fluid equations in a catchment model for flashfloods, debris flows and shallow slope failures. Environmental Modelling & Software **105**, 1–16.

Bryce, E., Lombardo, L., van Westen, C., Tanyas, H. and Castro-Camilo, D. (2022) Unified landslide hazard assessment using hurdle models: a case study in the Island of Dominica. Accepted in Stochastic Environmental Research and Risk Assessment .

Burton, A. and Bathurst, J. (1998) Physically based modelling of shallow landslide sediment yield at a catchment scale. Environmental Geology **35**(2), 89–99.

Catani, F. (2021) Landslide detection by deep learning of non-nadiral and crowdsourced optical images. Landslides **18**(3), 1025–1044.

Catani, F., Casagli, N., Ermini, L., Righini, G. and Menduni, G. (2005) Landslide hazard and risk mapping at catchment scale in the Arno River basin. Landslides **2**(4), 329–342.

Clinton, B. D. (2003) Light, temperature, and soil moisture responses to elevation, evergreen understory, and small canopy gaps in the southern appalachians. Forest ecology and Management **186**(1-3), 243–255.

Corominas, J., van Westen, C., Frattini, P., Cascini, L., Malet, J.-P., Fotopoulou, S., Catani, F., Van Den Eeckhaut, M., Mavrouli, O., Agliardi, F. et al. (2014) Recommendations for the quantitative analysis of landslide risk. Bulletin of engineering geology and the environment **73**(2), 209–263.

Davison, A. and Huser, R. (2015) Statistics of extremes. Annual Review of Statistics and Its Application **2**(1), 203–235.

Fawcett, T. (2006) An introduction to roc analysis. Pattern Recognition Letters **27**(8), 861–874. ROC Analysis in Pattern Recognition.

Fell, R., Corominas, J., Bonnard, C., Cascini, L., Leroi, E., Savage, W. Z. et al. (2008) Guidelines for landslide susceptibility, hazard and risk zoning for land-use planning. Engineering Geology **102**(3-4), 99–111.

Formetta, G., Capparelli, G. and Versace, P. (2016) Evaluating performance of simplified physically based models for shallow landslide susceptibility. Hydrology and Earth System Sciences **20**(11), 4585–4603.

Frattini, P., Crosta, G. and Carrara, A. (2010) Techniques for evaluating the performance of landslide susceptibility models. Engineering Geology **111**(1), 62–72.

Funk, C., Peterson, P., Landsfeld, M., Pedreros, D., Verdin, J., Shukla, S., Husak, G., Rowland, J., Harrison, L., Hoell, A. et al. (2015) The climate hazards infrared precipitation with stations—a new environmental record for monitoring extremes. Scientific data **2**(1), 1–21.

Guzzetti, F., Cardinali, M., Reichenbach, P. and Carrara, A. (2000) Comparing landslide maps: A case study in the upper tiber river basin, central italy. Environmental Management **25**(3), 247–263. 00000.

Guzzetti, F., Carrara, A., Cardinali, M. and Reichenbach, P. (1999) Landslide hazard evaluation: A review of current techniques and their application in a multi-scale study, central italy. Geomorphology **31**(1), 181–216.

He, K., Zhang, X., Ren, S. and Sun, J. (2015) Deep residual learning for image recognition. CoRR **abs/1512.03385**.

Heerdegen, R. G. and Beran, M. A. (1982) Quantifying source areas through land surface curvature and shape. Journal of Hydrology **57**(3-4), 359–373.

Huang, Y., Tang, Z., Chen, D., Su, K. and Chen, C. (2019) Batching soft IoU for training semantic segmentation networks. IEEE Signal Processing Letters **27**, 66–70.

Intrieri, E., Gigli, G., Mugnai, F., Fanti, R. and Casagli, N. (2012) Design and implementation of a landslide early warning system. Engineering Geology **147**, 124–136.

Ioffe, S. and Szegedy, C. (2015) Batch normalization: Accelerating deep network training by reducing internal covariate shift. CoRR **abs/1502.03167**.

Johnson, J. M. and Khoshgoftaar, T. M. (2019) Survey on deep learning with class imbalance. Journal of Big Data **6**(1), 1–54.

Ju, N., Huang, J., He, C., Van Asch, T., Huang, R., Fan, X., Xu, Q., Xiao, Y. and Wang, J. (2020) Landslide early warning, case studies from Southwest China. Engineering Geology **279**, 105917.

Kargel, J. S., Leonard, G. J., Shugar, D. H., Haritashya, U. K., Bevington, A., Fielding, E., Fujita, K., Geertsema, M., Miles, E., Steiner, J. et al. (2016) Geomorphic and geologic controls of geohazards induced by Nepal's 2015 Gorkha earthquake. Science **351**(6269), aac8353.

Kincey, M. E., Rosser, N. J., Robinson, T. R., Densmore, A. L., Shrestha, R., Pujara, D. S., Oven, K. J., Williams, J. G. and Swirad, Z. M. (2021) Evolution of coseismic and post-seismic landsliding after the 2015 Mw 7.8 Gorkha earthquake, Nepal. J Geophys Res Earth Surf **126**.

Kingma, D. P. and Ba, J. (2014) Adam: A method for stochastic optimization.

Kirschbaum, D. and Stanley, T. (2018) Satellite-Based Assessment of Rainfall-Triggered Landslide Hazard for Situational Awareness. Earth's Future **6**(3), 505–523.

Lee, S., Ryu, J.-H., Won, J.-S. and Park, H.-J. (2004) Determination and application of the weights for landslide susceptibility mapping using an artificial neural network. Engineering Geology **71**(3-4), 289–302.

Li, M., Zhang, X., Thrampoulidis, C., Chen, J. and Oymak, S. (2022) Autobalance: Optimized loss functions for imbalanced data. CoRR **abs/2201.01212**.

Loche, M., Scaringi, G., Yunus, A. P., Catani, F., Tanyaş, H., Frodella, W., Fan, X. and Lombardo, L. (2022) Surface temperature controls the pattern of post-earthquake landslide activity. Scientific reports **12**(1), 1–11.

Lombardo, L., Bakka, H., Tanyas, H., van Westen, C., Mai, P. M. and Huser, R. (2019) Geostatistical modeling to capture seismic-shaking patterns from earthquake-induced landslides. Journal of Geophysical Research: Earth Surface **124**(7), 1958–1980.

Lombardo, L., Opitz, T., Ardizzone, F., Guzzetti, F. and Huser, R. (2020) Space-time landslide predictive modelling. Earth-Science Reviews p. 103318.

Lombardo, L., Saia, S., Schillaci, C., Mai, P. M. and Huser, R. (2018) Modeling soil organic carbon with Quantile Regression: Dissecting predictors' effects on carbon stocks. Geoderma **318**, 148–159.

Lombardo, L. and Tanyas, H. (2020) Chrono-validation of near-real-time landslide susceptibility models via plug-in statistical simulations. Engineering Geology **278**, 105818.

Lombardo, L., Tanyas, H., Huser, R., Guzzetti, F. and Castro-Camilo, D. (2021) Landslide size matters: A new data-driven, spatial prototype. Engineering Geology **293**, 106288.

McAdoo, B. G., Quak, M., Gnyawali, K. R., Adhikari, B. R., Devkota, S., Rajbhandari, P. L. and Sudmeier-Rieux, K. (2018) Roads and landslides in Nepal: how development affects environmental risk. Natural Hazards and Earth System Sciences **18**(12), 3203–3210.

Meena, S. R., Soares, L. P., Grohmann, C. H., van Westen, C., Bhuyan, K., Singh, R. P., Floris, M. and Catani, F. (2022) Landslide detection in the Himalayas using machine learning algorithms and U-Net. Landslides pp. 1–21.

Monaco, S., Pasini, A., Apiletti, D., Colomba, L., Garza, P. and Baralis, E. (2020) Improving wildfire severity classification of deep learning U-nets from satellite images. In 2020 IEEE International Conference on Big Data (Big Data), pp. 5786–5788.

Moreno, M., Steger, S., Tanyas, H. and Lombardo, L. (2022) Modeling the size of co-seismic landslides via data-driven models: the kaikōura's example .

Nava, L., Bhuyan, K., Meena, S. R., Monserrat, O. and Catani, F. (2022) Rapid Mapping of Landslides on SAR Data by Attention U-Net. Remote Sensing **14**(6), 1449.

Neaupane, K. M. and Piantanakulchai, M. (2006) Analytic network process model for landslide hazard zonation. Engineering geology **85**(3-4), 281–294.

Nowicki Jessee, M., Hamburger, M., Allstadt, K., Wald, D., Robeson, S., Tanyas, H., Hearne, M. and Thompson, E. (2018) A Global Empirical Model for Near-Real-Time Assessment of Seismically Induced Landslides. Journal of Geophysical Research: Earth Surface **123**(8), 1835–1859.

Ohlmacher, G. C. (2007) Plan curvature and landslide probability in regions dominated by earth flows and earth slides. Engineering Geology **91**(2), 117–134.

Pearson, K. (1895) Note on regression and inheritance in the case of two parents. Proceedings of the Royal Society of London **58**, 240–242.

Prakash, N., Manconi, A. and Loew, S. (2021) A new strategy to map landslides with a generalized convolutional neural network. Scientific Reports **11**(1), 9722.

Qi, J., Du, J., Siniscalchi, S. M., Ma, X. and Lee, C.-H. (2020) On mean absolute error for deep neural network based vector-to-vector regression. IEEE Signal Processing Letters **27**, 1485–1489.

Reichenbach, P., Rossi, M., Malamud, B. D., Mihir, M. and Guzzetti, F. (2018) A review of statistically-based landslide susceptibility models. Earth-Science Reviews **180**, 60–91.

Richards, J., Huser, R., Bevacqua, E. and Zscheischler, J. (2022) Partially interpretable neural networks for high-dimensional extreme quantile regression: With application to wildfires within the mediterranean basin. Technical report, Copernicus Meetings.

Roback, K., Clark, M. K., West, A. J., Zekkos, D., Li, G., Gallen, S. F., Chamlagain, D. and Godt, J. W. (2018) The size, distribution, and mobility of landslides caused by the 2015 Mw7.8 Gorkha earthquake, Nepal. Geomorphology **301**, 121–138.

Ronneberger, O., Fischer, P. and Brox, T. (2015) U-net: Convolutional networks for biomedical image segmentation. CoRR **abs/1505.04597**.

Rosser, N., Kincey, M., Oven, K., Densmore, A., Robinson, T., Pujara, D. S., Shrestha, R., Smutny, J., Gurung, K., Lama, S. and Dhital, M. R. (2021) Changing significance of landslide hazard and risk after the 2015 mw 7.8 gorkha, nepal earthquake. Progress in Disaster Science **10**, 100159.

Samia, J., Temme, A. J., Bregt, A., Wallinga, J., Fausto Guzzetti, Ardizzone, F. and Rossi, M. (2017) Characterization and quantification of path dependency in landslide susceptibility. Geomorphology **292**, 16–24.

Scarselli, F., Gori, M., Tsoi, A. C., Hagenbuchner, M. and Monfardini, G. (2008) The graph neural network model. IEEE transactions on neural networks **20**(1), 61–80.

Shou, K.-J. and Lin, J.-F. (2020) Evaluation of the extreme rainfall predictions and their impact on landslide susceptibility in a sub-catchment scale. Engineering Geology **265**, 105434.

Sörensen, R., Zinko, U. and Seibert, J. (2006) On the calculation of the topographic wetness index: evaluation of different methods based on field observations. Hydrology and Earth System Sciences **10**(1), 101–112.

Srivastava, N., Hinton, G., Krizhevsky, A., Sutskever, I. and Salakhutdinov, R. (2014) Dropout: A simple way to prevent neural networks from overfitting. Journal of Machine Learning Research **15**(56), 1929–1958.

Steger, S., Mair, V., Kofler, C., Pittore, M., Zebisch, M. and Schneiderbauer, S. (2021) Correlation does not imply geomorphic causation in data-driven landslide susceptibility modelling–Benefits of exploring landslide data collection effects. Science of the total environment **776**, 145935.

Tanyaş, H., Allstadt, K. E. and van Westen, C. J. (2018) An updated method for estimating landslide-event magnitude. Earth surface processes and landforms **43**(9), 1836–1847.

Tanyaş, H., Görüm, T., Kirschbaum, D. and Lombardo, L. (2022a) Could road constructions be more hazardous than an earthquake in terms of mass movement? Natural Hazards .

Tanyas, H., Hill, K., Mahoney, L., Fadel, I. and Lombardo, L. (2021) The world's second-largest, recorded landslide event: lessons learnt from the landslides triggered during and after the 2018 Mw 7.5 Papua New Guinea earthquake .

Tanyaş, H., Hill, K., Mahoney, L., Fadel, I. and Lombardo, L. (2022b) The world's second-largest, recorded landslide event: Lessons learnt from the landslides triggered during and after the 2018 Mw 7.5 Papua New Guinea earthquake. Engineering Geology **297**, 106504.

Tanyaş, H., Kirschbaum, D., Görüm, T., van Westen, C. J., Tang, C. and Lombardo, L. (2021) A closer look at factors governing landslide recovery time in post-seismic periods. Geomorphology **391**, 107912.

Taylor, D. W. (1948) Fundamentals of Soil Mechanics. John Wiley & Sons.

Titti, G., Sarretta, A., Lombardo, L., Crema, S., Pasuto, A. and Borgatti, L. (2022) Mapping susceptibility with open-source tools: a new plugin for QGIS. Frontiers in Earth Sciences **229**.

Titti, G., van Westen, C., Borgatti, L., Pasuto, A. and Lombardo, L. (2021) When Enough Is Really Enough? On the Minimum Number of Landslides to Build Reliable Susceptibility Models. Geosciences **11**(11), 469.

Van Westen, C. J., Castellanos, E. and Kuriakose, S. L. (2008) Spatial data for landslide susceptibility, hazard, and vulnerability assessment: An overview. Engineering geology **102**(3-4), 112–131.

Wang, N., Cheng, W., Marconcini, M., Bachofer, F., Liu, C., Xiong, J. and Lombardo, L. (2022) Space-time susceptibility modeling of hydro-morphological processes at the Chinese national scale. Engineering Geology **301**, 106586.

Wang, X., Chen, Y. and Zhu, W. (2021) A survey on curriculum learning.

Weng, T.-W., Zhang, H., Chen, P.-Y., Yi, J., Su, D., Gao, Y., Hsieh, C.-J. and Daniel, L. (2018) Evaluating the robustness of neural networks: An extreme value theory approach. arXiv preprint arXiv:1801.10578 .

Whiteley, J., Chambers, J., Uhlemann, S., Wilkinson, P. B. and Kendall, J. (2019) Geophysical monitoring of moisture-induced landslides: a review. Reviews of Geophysics **57**(1), 106–145.

Worden, C. and Wald, D. (2016) ShakeMap manual online: Technical manual, user's guide, and software guide. US Geol. Surv. pp. 1–156.

Wu, H. and Gu, X. (2015) Max-pooling dropout for regularization of convolutional neural networks. CoRR **abs/1512.01400**.

Yesilnacar, E. and Topal, T. (2005) Landslide susceptibility mapping: a comparison of logistic regression and neural networks methods in a medium scale study, Hendek region (Turkey). Engineering Geology **79**(3-4), 251–266.

Zevenbergen, L. W. and Thorne, C. R. (1987) Quantitative analysis of land surface topography. Earth surface processes and landforms **12**(1), 47–56.

Zhang, Y., Chen, G., Zheng, L., Li, Y. and Wu, J. (2013) Effects of near-fault seismic loadings on run-out of large-scale landslide: a case study. Engineering geology **166**, 216–236.